Evidence of linear chirp in mid-infrared quantum cascade lasers: supplementary material

MATTHEW SINGLETON[1,*], **PIERRE JOUY**[1], **MATTIAS BECK**[1], **AND JÉRÔME FAIST**[1,†]

[1] *Institute for Quantum Electronics, ETH Zurich, 8093 Zürich, Switzerland*
[†] *e-mail: jfaist@phys.ethz.ch*
[*] *Corresponding author: smatthew@phys.ethz.ch*

This document provides supplementary information to "Evidence of linear chirp in mid-infrared quantum cascade lasers," https://doi.org/10.1364/OPTICA.5.000948.

1. ACQUISITION AND DATA TREATMENT

A 7.3 GHz RF tone (Rohde and Schwarz SMF 100A) is used as the local oscillator (LO) to downmix the amplified beatnote derived from the QCL, and the signal from the QWIP; these are then further downmixed and integrated on a fast (50 MS/s) lock-in amplifier (Zurich Instruments HF2LI), with an integration time corresponding to $\tau \approx 0.5\lambda_0/v$ (v the mirror velocity and λ_0 the central wavelength). A stabilised helium neon (HeNe) laser is also aligned to the interferometer (Brucker IFS 66/S), allowing the mirror displacement to be measured. This HeNe signal, the DC autocorrelation taken from the MCT, and lock-in signals are acquired on a 4-channel fast oscilloscope (LeCroy HDO6104). We generally oversample as far as the memory allows us, and then subsequently digitally filter the traces for a processing gain in SNR of a factor $\sqrt{N}$ for an oversampling factor N.

Care is taken to keep the coaxial cable lengths for the X and Y channels the same, as well as to use the identical filters, so as not to induce any artificial phase shifts between the components. Synchronisation between the DC autocorrelation and RF autocorrelation traces is achieved by comparing the positions of the centreburst (zero path difference) in the DC autocorrelation and the smallest peak in $|x(t) + iy(t)|^2$. As there is an AM component to the field oscillating at the repetition rate, as made clear by the existence of a measurable beatnote when light is shined directly onto the detector, such a peak must exist.

Zero crossings of the HeNe signal are identified, and linear interpolation is used to improve the precision in their estimate. The 3 single-sided interferograms are then resampled accordingly using a cubic interpolator. We thus move from units of the scope's internal LO t to the relative path delay τ. Being considered narrowband signals (fractional bandwidth < $100cm^{-1}/1200cm^{-1} \approx 8.4\%$), phase correction steps are deemed unnecessary.

The interferograms are then apodised using the Mertz window [1], zero-padded, left circular shifted to the centreburst, and Fourier transformed, as is conventionally done for single-sided interferograms. A first estimate of the comb repetition rate is then found either by adding the lock-in demodulation frequency to the LO frequency used for the downconversion, which is usually selected to be below the fundamental beat tone of the QCL, or by measuring the delay in the interferogram from the centreburst to the first satellite. The estimate is then improved iteratively on the DC autocorrelation spectrum, which generally has a higher SNR, by choosing the values of $\hat{\omega}_0$ and $\hat{\omega}_r$ which maximise $\sum_n I(\hat{\omega}_0 + n\hat{\omega}_r)$.

For stability, we made use of a low-noise current driver (Wavelength Electronics QCL2000) and thermoelectric cooler (Wavelength Electronics PTC 10 K-CH, with a standard Peltier element), in combination with an RF self-referencing scheme to mitigate drift. To verify the stability, we measured the deviation of the signal from the lock-in at a fixed path difference at rapid intervals over the course of more than 20 minutes. As shown from the Allan deviation[2] in Fig. S1 (a), there is no obvious drift in the signal over 100 seconds. The stability is confirmed in Fig. S1 (b), where superimposed are 13 amplitude and phase difference traces, for measurements taken sequentially at the same operating point with no power cycling in-between. As can be seen, they are very consistent and one can legitimately average.

Confidence intervals are found by the following procedure[3]. The noise level is estimated by taking the average out-of-band power, i.e. in spectral regions seen to contain no signal. This is then taken as $\hat{\sigma}_N^{(dc)}$ for the DC spectrum, and $\hat{\sigma}_N^{(c,r)}$, $\hat{\sigma}_N^{(c,i)}$ for the real and imaginary quadratures of the complex spectra ($c = X - iY$), respectively. Monte-Carlo simulations are then run, whereby samples for $dc(\omega_n)$, $c_r(\omega_n)$, $c_i(\omega_n)$ are drawn, and

matching values for A, ϕ are calculated, forming a unique spectrum. For each configuration, the field is simulated. Finally from the ensemble, the expectation and $\sigma_{N95\%}$ confidence bounds for the instantaneous frequency and intensity are extracted.

(a)

(b)
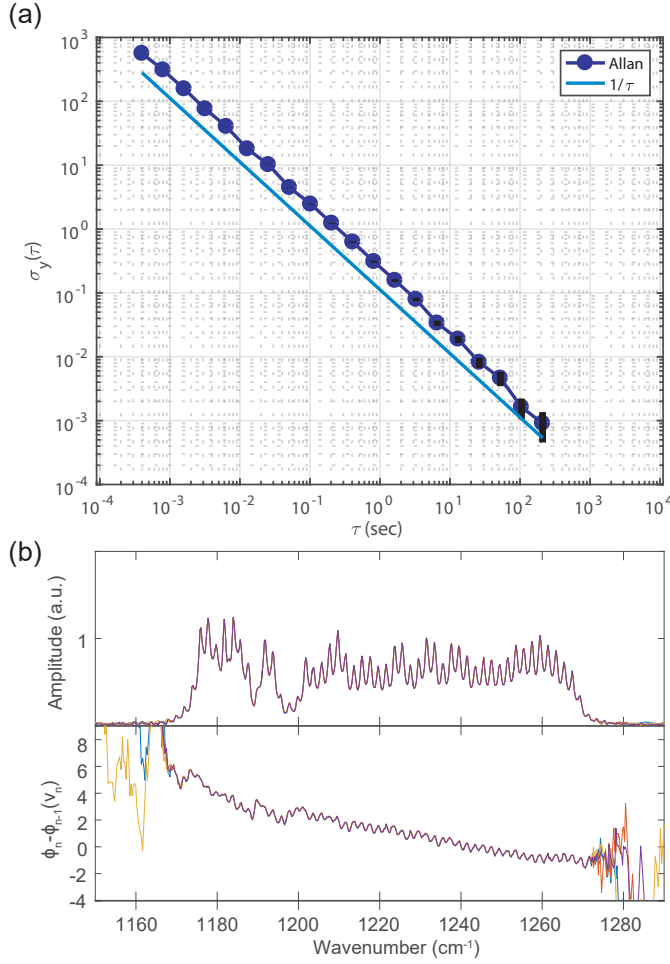
Fig. S1. (a) Allan deviation[2] measured with the mirror at a fixed position, for a maximum delay of 200 s. (b) Repeat measurements of the phase differences taken over the course of 5 minutes, at a single operating point, with no power cycling between, and treated identically. The results have a median spread of about 15 mrad, demonstrating the phase stability of the comb.

2. SAMPLES AND FURTHER ANALYSIS

Two similar devices were characterised for this paper, of the same active region EV2429, and process B: 21NU, and 26HM. Both devices have a high-reflectivity coating on the back facet (300 nm Al2O3, 150 nm Au). The GVD for 21NU is shown in Figure S3 (a). It varies from around -200 to -400 fs^2/mm, and appears to cross zero at around 1175 cm^{-1}. At 1275 cm^{-1} there seems to be another turning point. The values for the 26HM in Figure S3 (b) show similar features and values.

The second device, 26 HM, also demonstrates this chirping behaviour, with the difference in group delay between the left and the right lobes also appearing. Measurements of the modal amplitudes and corresponding group delay are shown in Fig. S5 (a) for 1.2931 A and (c) for 1.6414 A. As before, the time dependent

(a)

(b)

(c)
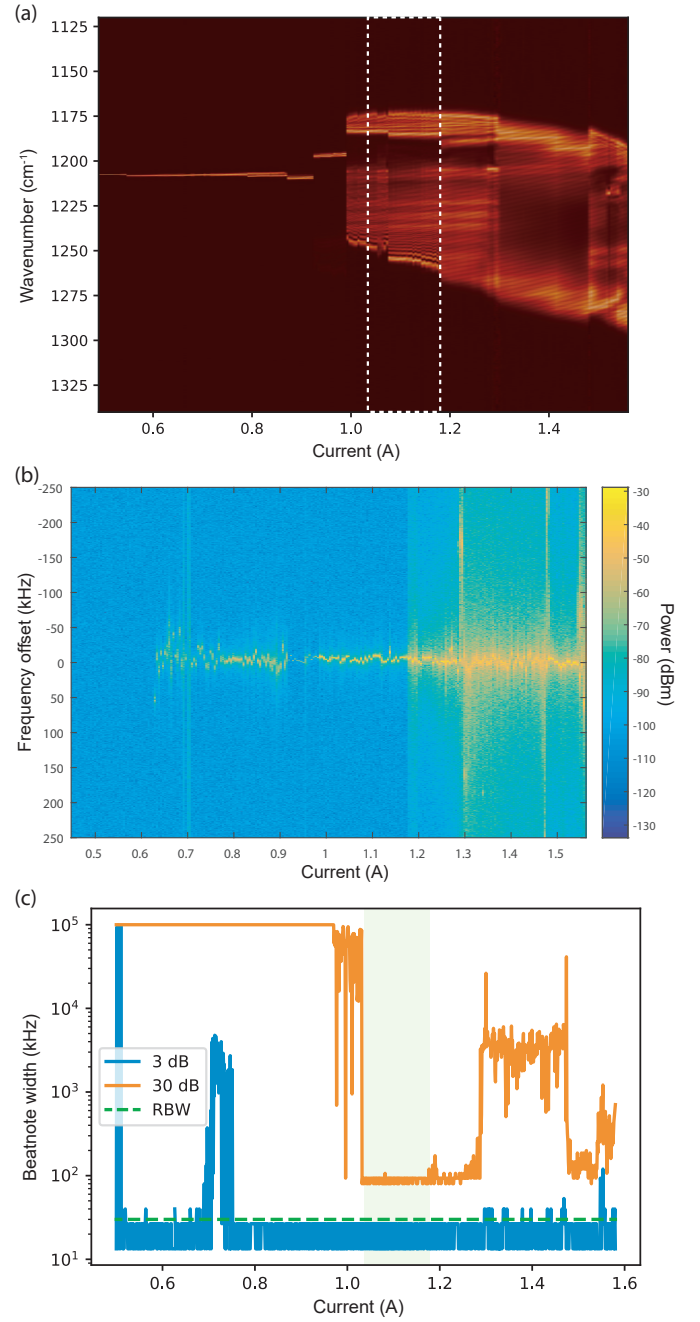
Fig. S2. Device characteristics for sample 21NU. (a) Spectral map taken at 291 K, linear scale. The individual spectra are normalised to the maximum, with lighter colours indicating higher intensity. (b) Beatnote map, taken at a resolution bandwidth (RBW) of 500 Hz. (c) Beatnote width measured at 3 dB (FWHM, blue) and 30 dB (orange, intending to capture the pedestal) at RBW 3 kHz (green dashed line). The shaded green area covering 1.05 - 1.18 A marks the region over which the laser is operating as a quiet frequency comb. Not shown: the green shaded region was measured to have the lowest jitter. Though the pedestal dip around 1.55 A would seem like a candidate state to measure, lasing in this region produces more than 10 times the frequency noise and relative intensity noise.

intensity and instantaneous frequency are also plotted in (b) and (d). This further shows that the chirped state persists, or at least

(a) Device: 21 NU

(b) Device: 26 HM
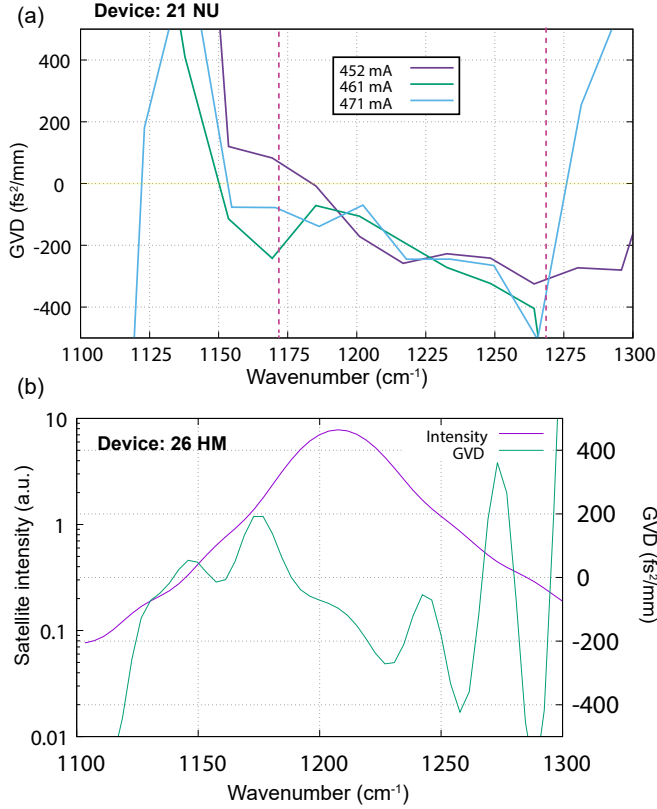
Fig. S3. GVD of the two devices measured subthreshold at 298 K using the Hakki-Pauli method[4]. (a) Sample 21 NU: GVD at 3 different current setpoints, giving an estimated GVD of -200 fs^2 at the spectral centre. The pink dashed lines indicate the approximate spectral width where the phases were measured. Note the positive going zero crossing at the red side (1170 cm^{-1}) of the spectrum, and the apparent turning point on the blue side at around 1170 cm^{-1}. (b) GVD for the 26 HM device, at a resolution of 31.6 cm^{-1}. The purple line indicates the intensity of the spectrum of the first satellite, giving an indication of the range over which the measurement can be trusted. The blue curve gives the GVD, seen to be around -100 fs^2.

exists at multiple points, even over a larger current range than that measured for the first device.

Note that the plotted instantaneous frequency in places shows rapid swings between two extrema. This is partly an artefact of the 1D representation, and corresponds to multiple separated spectral components with similar group delay, with different time-dependent weightings. The spectrogram in Fig. S6, shows exactly this behaviour, with the two distinct GDDs for the two lobes plainly visible, and the overlapping components at around 25 ps.

Such a temporal response shows it something of an oversimplification to describe the field as a plain linear chirp. Plotted in Fig. S7 (a) are the intermodal phase differences, from which the overall GDD was estimated for the 21NU device. Looking more closely, in particular at the highest current values, one can see that there is in fact higher order dispersion present in the field. This seems to manifest itself in three distinct regions: the lobe to the left of 1200 cm^{-1}; the broader region to the right of 1200 cm^{-1}; and those new frequency components which grow
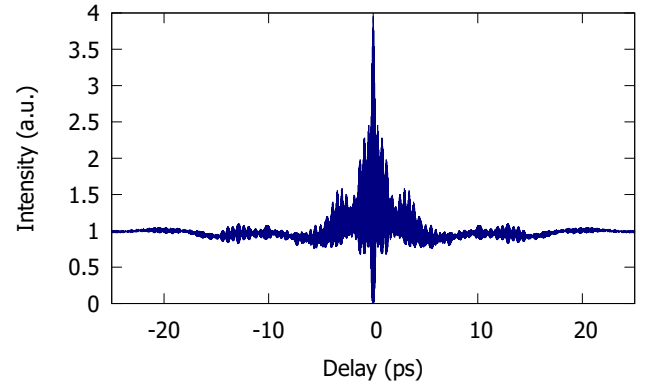
Fig. S4. Simulated interferometric autocorrelation $I(\tau) = \int_{-\infty}^{+\infty} |(E(t) + E(t-\tau))^2|^2 dt$, computed with the field in Figure 2 in the main text. The peak to background ratio of 4:1 is consistent with the that presented in[5], where they directly measured the $g^{(2)}$ of a device lasing at 8 μm using a two-photon QWIP.

from the main comb towards the blue. In (b), we perform 3 crude linear fits to these fixed spectral regions, and in (c) plot the estimated GDD as a function of current. The left lobe seems to have a GDD approximately twice that of the central region, while the right lobe has surprisingly a negative GDD of about the magnitude as the middle. As the current increases (i.e. the spectrum grows), the 3 values seem to all decrease in magnitude, though at no point do they reconcile.

3. MERIT FUNCTION

We refer interested readers to [6] for a full discussion of the model.

The merit function is calculated as follows. Firstly, the FWM term on the RHS of S5 is computed for an amplitude spectrum of fixed magnitude, but swept chirp. In the second step, the overall merit is computed, including an adjustable parameter $\tilde{\alpha}$, which is set such that the difference between the LH terms and RH terms is minimised; the position of optimal chirp coincides with this term being maximised, the ultimate value of which can be interpreted as a measure of the efficiency of the lasing state.

The modal amplitudes take on an assumed shape, in this particular case a sum of 3 Gaussians, but the total optical power is left as a free parameter by letting $\tilde{A}_n = \alpha A_n$.

If we let

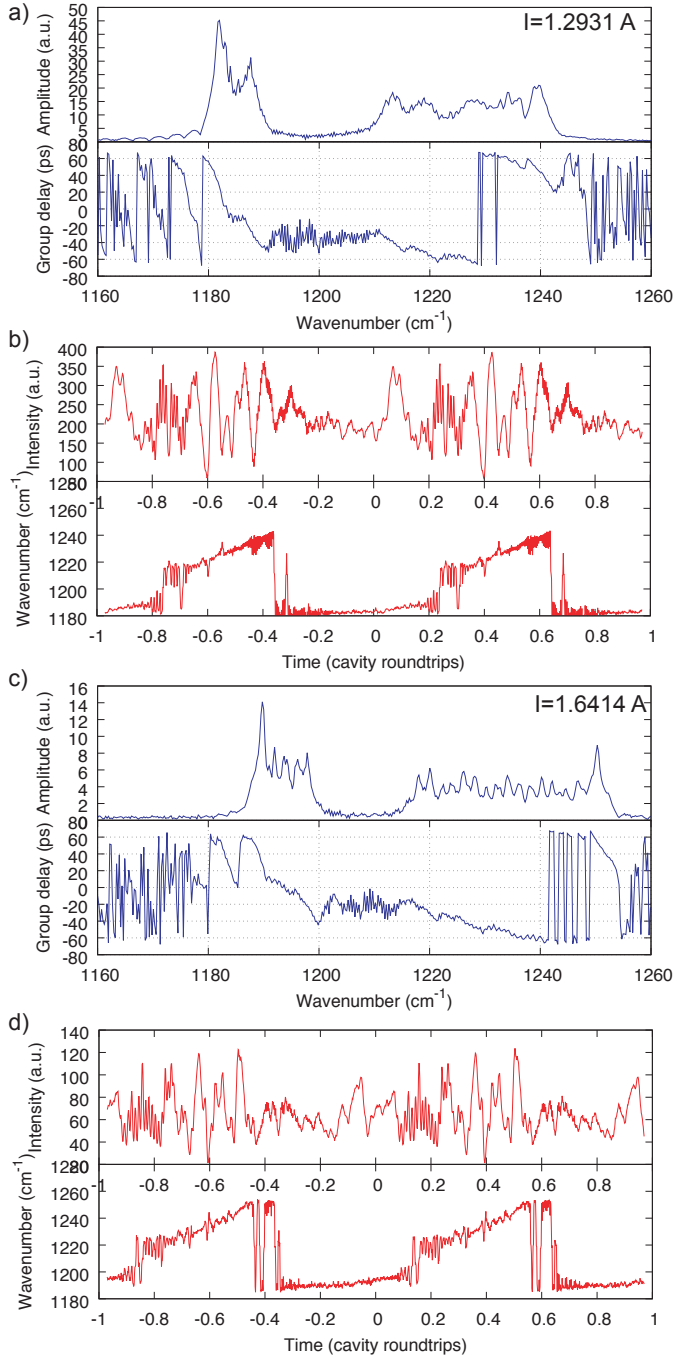$$S_n = \sum_{k,l=-N/2}^{N/2} A_m A_k A_l^* B_{kl} C_{kl} \kappa_{n,l,k,m} \tag{S1}$$

be the FWM sum, where

$$C_{kl} = \frac{\gamma_{22}}{\gamma_{22} - i(k-l)\omega} \tag{S2}$$

$$B_{kl} = \frac{\gamma_{12}}{2i} \left(\frac{1}{-i\gamma_{12} - l\omega} - \frac{1}{i\gamma_{12} - k\omega} \right) \tag{S3}$$

$$\kappa_{n,l,k,m} = \begin{cases} \frac{3}{8}, & k = l = n, \\ \frac{1}{4}, & k = l \neq n \text{ or } l = n, \\ \frac{1}{8}, & \text{otherwise} \end{cases} \tag{S4}$$

we then have the following merit function:

Fig. S5. (a), (b) Modal amplitudes and phase differences, scaled to the comb repetition rate to give the group delay, for 26HM, measured at 1.2931 A and 1.6414 A, respectively. (c) and (d) Extracted intensity and instantaneous frequency. Note that, for these traces there was no averaging, and so the SNR is generally poorer, as most apparent near the centre of the spectrum.

$$M(\alpha, c) = \sum_n \left| (G_n - 1)\tilde{\alpha} A_n - \tilde{\alpha}^3 G_n S_n \right|^2 \quad (S5)$$

Where the objective is to minimise $M(\alpha, c)$. We neglect the dispersion term for this analysis.

In Fig. S8 (a), we have plotted the merit function over a larger
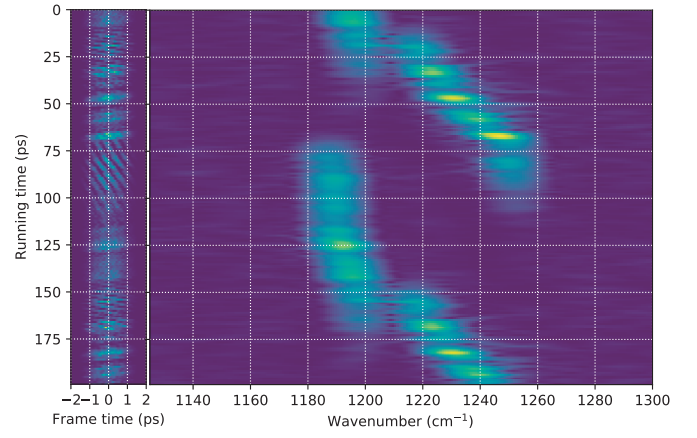
Fig. S6. Spectrogram computed for Fig. S5 (d). Left: time slices (5 ps frame time). Right: Corresponding Fourier spectrum.

extent of chirp parameter, demonstrating that there are many values of chirp which minimise Eqn. S5. One such state is depicted in (c), which makes 4 complete frequency sweeps per round-trip.

4. DISSIPATION

As described by M. Piccardo, D. Kazakov et. al. [7], the optical field induces a spatiotemporal population grating in the device, externally measurable by probing across the length of the laser ridge the radio frequency voltage, oscillating at the intermodal beat frequencies. We propose that such a voltage grating would induce in-plane currents in the high-conductivity cladding and contact layers, which would contribute to the loss through ohmic dissipation.

We begin by describing the intracavity field as a sum of forward and backward propagating waves $E = E_f + E_b$, assuming no mirror losses:

$$E_f = \sum_n A_n e^{i(\omega_n t + k_n x)} \quad (S6)$$

$$E_b = \sum_n A_n e^{i(\omega_n t - k_n x)} \quad (S7)$$

The intensity is then EE^* as usual:

$$I(x,t) = (E_f + E_b)(E_f + E_b)^* = E_f E_f^* + E_b E_b^* + E_f E_b^* + c.c. \quad (S8)$$

The cross terms $E_f E_b^*$ give rise to sum spatial frequency terms on the order of the optical wavelength. We hence neglect these, as such terms will not induce currents in the cladding. We then have:

$$I(x,t) = \sum_m \sum_n A_n A_m^* \left[e^{-i(n-m)\omega_r t} e^{i(k_n - k_m)x} + e^{i(n-m)\omega_r t} e^{i(k_n - k_m)x} \right] \quad (S9)$$

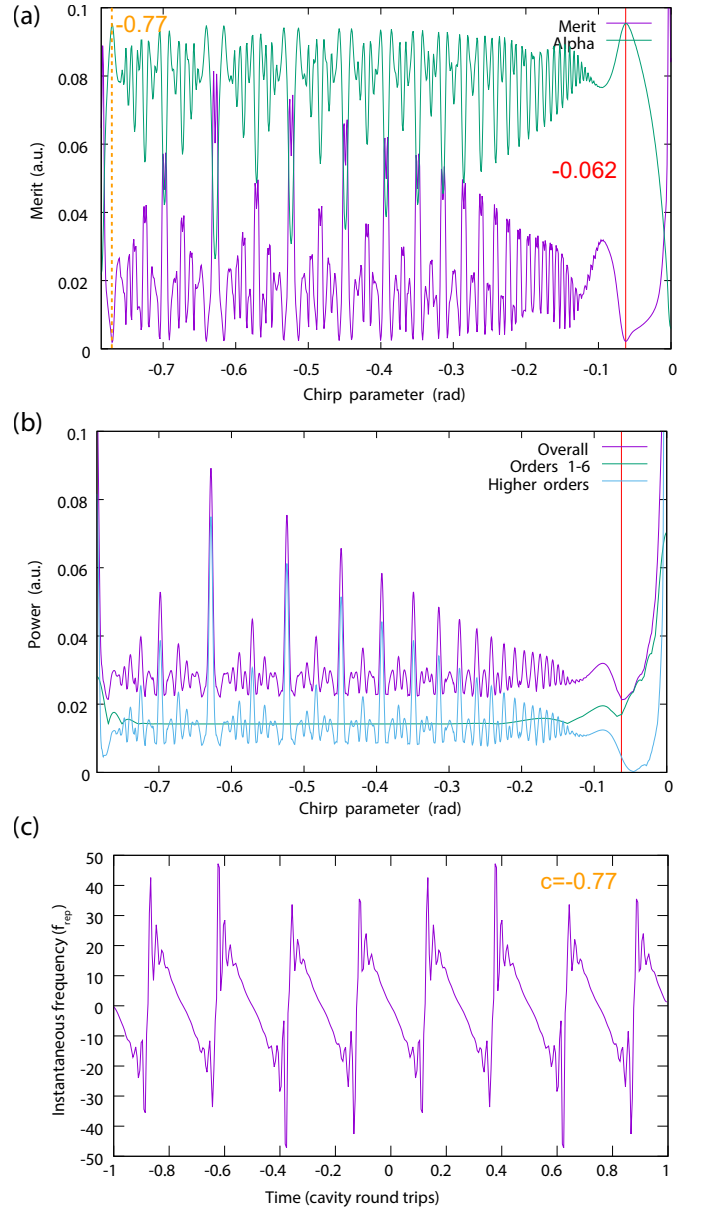If we then look at only those terms which oscillate at $b\omega_r$ (i.e. $m = n + b, m = n - b$):

$$\langle I(x,t) \rangle|_{b\omega_r} = \sum_n A_n [A_{n-b}^* e^{-ib\omega_r t} e^{i(k_n - k_{n-b})x} +$$
$$A_{n+b} e^{ib\omega_r t} e^{i(k_n - k_{n+b})x} +$$
$$A_{n-b}^* e^{ib\omega_r t} e^{i(k_n - k_{n-b})x} +$$
$$A_{n+b}^* e^{-ib\omega_r t} e^{i(k_n - k_{n+b})x}] \quad (S10)$$

(a)

(b)

(c)
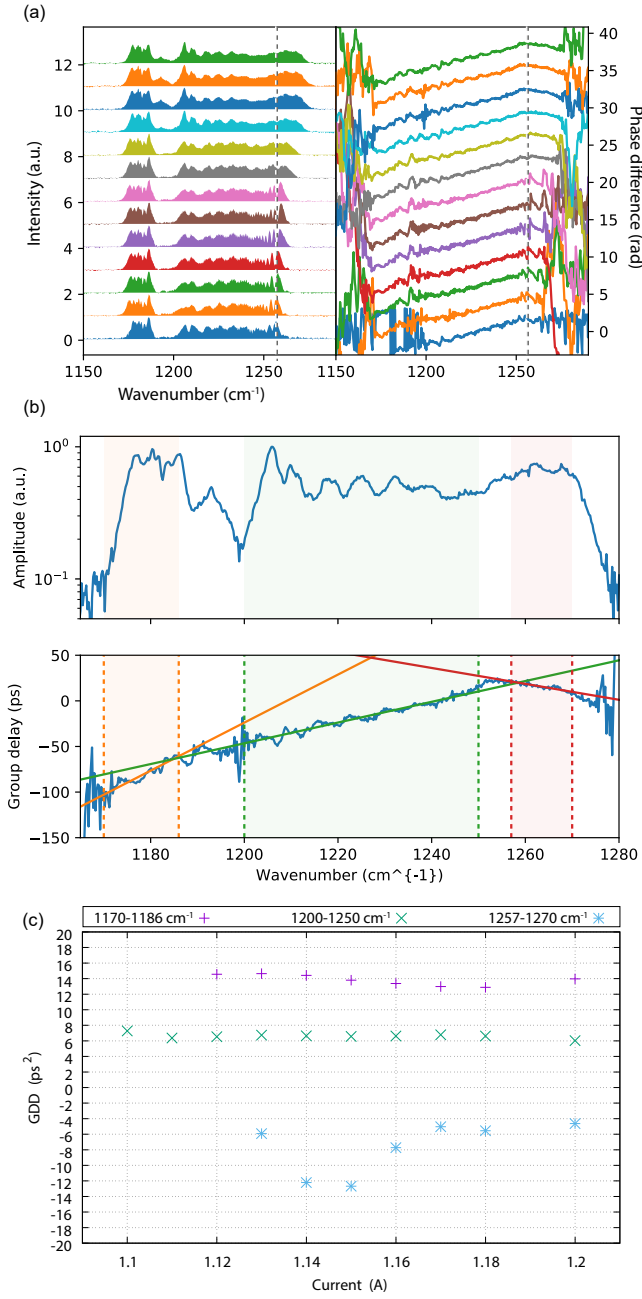
Fig. S7. (a) Amplitude spectrum (left) and phase differences (right) measured as a function of current for device 21NU. The current increases in 10 mA steps, going from the bottom up. The blue dashed line indicates where the GVD changes from negative from positive. (b) Linear fit of group delay at the lobes 1170-1186 cm^{-1} (orange), 1200-1250 cm^{-1} (green), and 1257-1270 cm^{-1} to estimate the GDD of the 3 distinct regions, plotted for 1.20 A. (c) Corresponding GDD estimates for all current values.
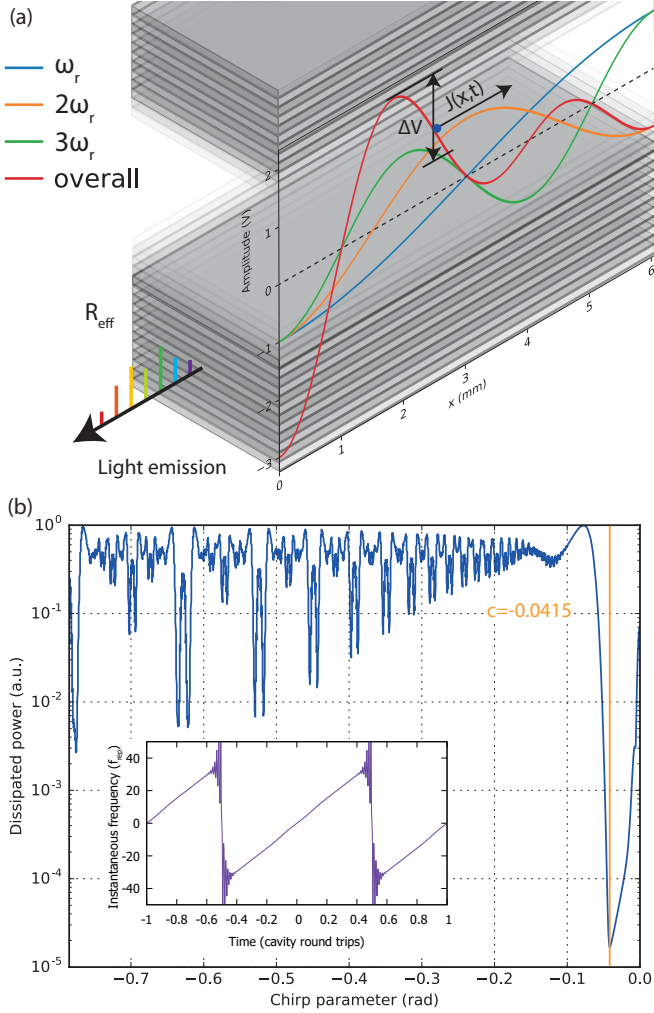
(a)

(b)

(c)

Fig. S8. (a)Merit plotted for an extended range, showing the multiplicity of chirped solutions. Powers of low frequency (up to order 6) and high frequencies is superimposed, showing the sharp increase of high order beating terms, which we propose to induce losses. The red dashed line indicates a higher chirped state, for which the instantaneous frequency is plotted in (c). (b) Beating terms $\sum_n A_n A_{n+B}^*$, where B is the beating order, computed as a function of the chirp parameter. The low and high orders of B are separated to highlight that high frequency beatings only play a role for higher chirped states.

$$\langle I(x,t)\rangle|_{b\omega_r} = \cos(b\omega_r t)\sum_n A_n \left[A_{n-b}^* e^{ibk_r x} + A_{n+b}^* e^{-ibk_r x}\right] \tag{S11}$$

$$\langle I(x,t)\rangle|_{b\omega_r} = \cos(bk_r x)\cos(b\omega_r t)\sum_n A_n A_{n-b}^* + c.c. \tag{S12}$$

The intra-cavity intensity will induce a population grating,

Which, with the spatial repetition rate $k_r = 2\pi(\frac{1}{\lambda_n} - \frac{1}{\lambda_{n-1}})$, conveniently simplifies to:

(a)

(b)

Fig. S9. (a) QCL active region, with an intracavity field. Plotted are the intensity gratings at some fixed time t_0 for the fundamental and second and third harmonic of the intermodal beat frequency, and the sum of the 3. This is assumed to directly correspond to a voltage, which induces a current $\Delta V(x,t)R_{eff}$ (shown by the arrow) which varies spatiotemporally. (b) Dissipative loss, calculated for the same spectrum as in the main paper, as a function of chirp. This is scaled to α^2, as in Fig. S8 (a).

which tracks these intensity beatings[7]. As such, a spatiotemporally varying voltage will also exist, which we assume to run perfectly in phase with the driving intensity. This can therefore be expressed:

$$V(x,t) = IR_{eff} \propto EE^* \qquad (S13)$$

where R_{eff} can be seen as an effective, or average, resistance, as experienced by the current passing through the structure in-plane. The situation is depicted in Fig. S9 (a), where the instantaneous potential difference $V(x_0 + \delta, t) - V(x_0, t)$ is seen to induce a current density $J(x_0, t)$. We hence take the spatial derivative in the direction of propagation:

$$\frac{dV(x,t)|_{b\omega_r}}{dx} = -bk_r \sin(bk_r x)\cos(b\omega_r t) + c.c. \qquad (S14)$$

The power dissipated by order b is therefore proportional to:

$$P_{diss}^{(b)} \propto b^2 K_r^2 \int \int \sin^2(bk_r x)\cos^2(b\omega_r t)dxdt \qquad (S15)$$

i.e., the loss scales with the square of the beating frequency. Now, with reference to beating map shown in Section 3 of the Main Text, one might therefore expect these losses to increase after around $c = -0.05$, when the fast oscillations start to set in. By summing across all beats, we find the overall dissipation to be:

$$P_{diss} = \frac{1}{T}\int_0^T \int_0^L \left(-\sum_b \sin(bk_r x)\cos(b\omega_r t)\sum_n A_n A_{n-b}^* + c.c.\right)^2 dxdt \qquad (S16)$$

In Fig.S9 (b), we present this dissipation as a function of chirp. Under the assumptions we have made, one can see a clear penalty of a factor more than 100 directly attributable to the additional dissipation when lasing at a higher chirped state, which was not apparent from the merit function alone; indeed, the minimum is also slightly shifted towards a lower chirp of $c = -0.0415$. However, we should be careful in drawing conclusions from this, in that we have yet to quantify in real units the order of magnitude of this effect, and we have furthermore treated the active region as having a fixed effective resistance, rather than a frequency dependent impedance, which will no doubt again affect the weightings of the individual beating components. These need to be considered more carefully in a future work. Nonetheless, this idea of intracavity field intensity induced loss may go some way to explaining why the laser opts for a lower chirped state, where we have only one frequency sweep per round trip.

REFERENCES

1. L. Mertz, "Auxiliary computation for Fourier spectrometry," Infrared Phys. **7**, 17–23 (1967).
2. D. W. Allan, "Statistics of atomic frequency standards," Proc. IEEE **54**, 221–230 (1966).
3. D. Burghoff, Y. Yang, D. J. Hayton, J.-R. Gao, J. L. Reno, and Q. Hu, "Evaluating the coherence and time-domain profile of quantum cascade laser frequency combs," Opt. Express **23**, 1190 (2015).
4. D. Hofstetter and J. Faist, "Measurement of semiconductor laser gain and dispersion curves utilizing Fourier transforms of the emission spectra," IEEE Photonics Technol. Lett. **11**, 1372–1374 (1999).
5. A. Gordon, C. Y. Wang, L. Diehl, F. X. Kärtner, A. Belyanin, D. Bour, S. Corzine, G. Höfler, H. C. Liu, H. Schneider, T. Maier, M. Troccoli, J. Faist, and F. Capasso, "Multimode regimes in quantum cascade lasers: From coherent instabilities to spatial hole burning," Phys. Rev. A **77** (2008).
6. G. Villares and J. Faist, "Quantum cascade laser combs: effects of modulation and dispersion," Opt. Express **23**, 1651 (2015).
7. M. Piccardo, D. Kazakov, N. A. Rubin, P. Chevalier, Y. Wang, F. Xie, K. Lascola, A. Belyanin, and F. Capasso, "Time-dependent population inversion gratings in laser frequency combs," Optica **5**, 475–478 (2018).